Title: Receptor interacting protein kinase-3 mediates both myopathy and cardiomyopathy in preclinical animal models of Duchenne muscular dystrophy

Maximilien Bencze[1] ✉ , Baptiste Periou[1] , Isabel Punzón[1], Inès Barthélémy[1], Valentina Taglietti[1], Cyrielle Hou[1], Louai Zaidan[1], Kaouthar Kefi[1], Stéphane Blot[1], Onnik Agbulut[2], Marianne Gervais[1], Geneviève Derumeaux[3], Laurent Tiret[1], François-Jérôme Authier[1], Fréderic Relaix[1]

[1] U955-IMRB, Inserm, UPEC, ENVA, EFS, Team 10, Biology of the Neuromuscular System, Créteil 94000, France.

[2] Sorbonne Université, Institut de Biologie Paris-Seine (IBPS), CNRS UMR 8256, Inserm ERL U1164, Biological Adaptation and Ageing, 75005, Paris-France.

[3] U955-IMRB, Université Paris-Est Créteil (UPEC), Team 8, Department of Physiology, Henri Mondor Hospital, FHU-SENEC, AP-HP, Créteil, France.

✉ **Correspondence:** Maximilien Bencze: maximilien.bencze@inserm.fr, m.bencze@ucl.ac.uk

Keywords: Duchenne muscular dystrophy, myonecrosis, programmed cell death, necroptosis, fibrosis, myogenesis, cardiac failure, animal model.

Abstract

Background

Duchenne muscular dystrophy (DMD) is a progressive muscle degenerative disorder, culminating in a complete loss of ambulation, hypertrophic cardiomyopathy and a fatal cardiorespiratory failure. Necroptosis is the form of necrosis that is dependent upon the receptor-interacting protein kinase (RIPK) 3; it is involved in several inflammatory and neurodegenerative conditions. We previously identified RIPK3 as a key player in the acute myonecrosis affecting the hindlimb muscles of the dystrophic mouse model, mdx. Whether necroptosis also mediates respiratory and heart disorders in DMD is currently unknown.

Methods

Evidence of activation of the necroptotic axis was examined in dystrophic tissues from Golden retriever muscular dystrophy (GRMD) dogs and R-DMDdel52 rats. A functional assessment of the involvement of necroptosis in dystrophic animals was performed on mdx mice that were genetically depleted for RIPK3. Dystrophic mice aged from 12 to 18 months were analyzed by histology and molecular biology to compare the phenotype of muscles from mdx*Ripk3*$^{+/+}$and mdx*Ripk3*$^{-/-}$ mice. Heart function was also examined by echocardiography in 40-week-old mice.

Results

Quantification of *RIPK3* transcripts in sartorius and biceps femoris muscles from GRMD dogs positively correlated to myonecrosis levels (r=0.81; p=0.0076). *RIPK3* was also found elevated in the diaphragm (p=0<0.05). In the slow progressing heart phenotype of GRMD dogs, the phosphorylated form of RIPK1 at the Serine 161 site was dramatically increased in cardiomyocytes. A similar p-RIPK1 upregulation characterized the cardiomyocytes of R-DMDdel52 rats, associated with a marked overexpression *of Ripk1* (p=0.007) and *Ripk3* (p=0.008), indicating primed activation of the necroptotic pathway in the dystrophic heart. Mdx*Ripk3*$^{-/-}$ mice displayed decreased compensatory hypertrophy of the heart (p=0.014), and echocardiography showed a 19% increase in the relative wall thickness (p<0.05) and 29% reduction in the left ventricle mass (p=0.0144). Besides, mdx*Ripk3*$^{-/-}$ mice presented no evidence

of a regenerative default or sarcopenia in skeletal muscles, moreover around 50% less affected by fibrosis ($p<0.05$).

Conclusions

Our data provide evidence of the activation of the necroptotic pathway in degenerative tissues from dystrophic animal models, including the diaphragm and the heart. The genetic inhibition of necroptosis in dystrophic mice improves both cardiac function and histological features of muscles, suggesting that prevention of necroptosis is susceptible to providing multiorgan beneficial effects for DMD.

57 # Introduction

58 Duchenne muscular dystrophy (DMD) is an X-linked genetic disorder, affecting 1/5000 male birth
59 worldwide. Loss-of-function mutations in the dystrophin gene primarily lead to chronic myofibre
60 necrosis (myonecrosis) and severe locomotor muscle disability starting in early childhood. Notably, the
61 absence of dystrophin at the sarcolemma renders myofibre more susceptible to mechanical stress, which
62 favours contraction-induced myonecrosis. Following injury, muscle repair requires myogenesis thanks
63 to the contribution of PAX7-expressing resident muscle stem cells (MuSC)[1]. However, in disabling
64 neuromuscular disorders involving chronic myofiber degeneration such as DMD, regeneration does not
65 fully compensate for chronic myofibre demise. The loss of a sustained homeostatic balance between the
66 two mechanisms leads to the increasing replacement of contractile myofibres by fibrotic or adipose
67 tissue. Biopsies with interstitial fibrosis positively correlate with a poor outcome in DMD boys [2]. Thus,
68 identifying the molecular pathways involved in fibrosis formation is relevant for improving therapeutic
69 perspectives. Dystrophin deficiency also challenges the survival of respiratory and cardiac muscle cells,
70 leading to the premature death of DMD patients from cardiorespiratory weakness or failure [3,4].
71 Recently, we reported that necroptosis, a receptor-interacting protein kinase (RIPK)1- RIPK3- and
72 mixed lineage domain kinase-like (MLKL)-dependent cell death pathway, is activated in the locomotor
73 musculature of murine dystrophin-deficient muscles. Necroptosis inhibition dampens the peak of
74 myonecrosis in the locomotor muscles of three-week-old mdx mice and improves muscle function in
75 young adults [5]. However, two recent studies reported a link between necroptosis inhibition and a deficit
76 in early myogenesis and myofibre atrophy[6,7]. One of them reported that RIPK3 depletion in mdx MuSCs
77 dramatically impairs muscle function. Repressing necroptosis might therefore lead to two putative
78 conflictual outcomes: a decrease in myofibre degeneration, together with a default in muscle
79 regeneration leading to muscle atrophy and sarcopenia. Consequently, the long-term effects of
80 necroptosis inhibition in dystrophic skeletal and heart muscle remodelling need to be determined, before
81 further envisaging the necroptotic pathway as a putative therapeutic target for DMD.
82 To this end, we examined the diaphragm and heart for evidence of necroptosis activation from Golden
83 retriever muscular dystrophy (GRMD) dogs. The functional assessment of necroptosis in the

84 cardiorespiratory system was achieved using mdx*Ripk3*$^{-/-}$ mice. Compared to mdx*Ripk3*$^{+/+}$, locomotor
85 muscles from mdx*Ripk3*$^{-/-}$ mice displayed a significant reduction of fibrosis. Despite its involvement in
86 early myogenesis, RIPK3 deficiency did not generate sarcopenia. In the diaphragm, fibrosis reduction
87 indicates that necroptosis not only participates in the pathology of limbs, but also of respiratory muscles.
88 Importantly, we found that RIPK3 depletion improves cardiomyopathy by reducing heart hypertrophy
89 and fibrosis deposition. Together, our data demonstrate that in dystrophic mdx mice, RIPK3 is
90 dispensable for post-lesional myogenesis and suggests that necroptosis inhibition is beneficial on the
91 hindlimb, respiratory, and heart muscles in dystrophinopathies. This work opens new avenues for further
92 research exploring the improvement of patients' health status by reducing necroptosis.
93

94 # Material and methods

95 **Animals**

96 Mice and rats were bred in the Institut Mondor de Recherche biomédicale, Créteil, France in a pathogen-
97 free facility with 12-h light and 12-h dark cycles in accordance with European Directive 2010/63/EU.
98 Only male mice and rats were used for the experiments. Both wild-type (WT) and DMD rats and mdx
99 mice were born from the same litter. The GRMD dogs included in this study were housed in the facilities
100 of the neurobiology laboratory of the Veterinary School of Alfort. Experiments were approved by the
101 Anses/EnvA/Upec Ethics Committee. All care and manipulations were performed by national and
102 European legislation on animal experimentation. *Ripk3*$^{-/+}$ mice were kindly provided by Genentech (San
103 Francisco-CA). mdx*Ripk3*$^{-/-}$ mice were generated by crossing *Ripk3*$^{-/-}$ with mdx mice. The resulting mice
104 were backcrossed for at least four generations to obtain final mdx*Ripk3*$^{+/-}$ breeders.
105

106 **Treadmill tests**

107 The running capacity was evaluated on a treadmill (Tecmachine, Medical Development) at a +5% slope.
108 Males of 70- to 76-week-old mice were initially acclimatized to the treadmill for 5 days (10 min/day
109 and 12 m/min). Mice were challenged to an exercise of progressively increased intensity. Speed was
110 increased every 90- to 120 seconds/min and the speed of the last completed running step before
111 exhaustion was considered as the individual maximal aerobic speed.

112
113 **RNA extraction, PCR, and real-time PCR**

114 Total skeletal muscle RNA was extracted from muscle and heart samples using TRIzol (Thermo Fisher
115 Scientific) following the manufacturer's instructions. SuperScript III Reverse Transcriptase from the
116 Invitrogen kit converted RNA into cDNA using the Veriti 96- Well Fast Thermal Cycler (Applied
117 Biosystems). Gene expression was quantified by real-time qPCR with the StepOnePlus real-time PCR
118 system (Applied Biosystems) using SYBR Green detection tools (Applied Biosystems). In skeletal
119 muscle tissue, the expression of each gene was normalized to *Tbp* gene expression. Results are reported
120 as relative gene expression (2-DDCT). In the heart, from 500 ng of extracted RNA, the first-
121 strand cDNA was then synthesized using a RevertAid First Strand cDNA Synthesis Kit (Thermo
122 Fisher Scientific) with random hexamers according to the manufacturer's instructions. Using the Light
123 Cycler® 480 system (Roche Diagnostics), the reaction was carried out in duplicate for each sample in a
124 6-µl reaction volume containing 3 µl of SYBR Green Master Mix, 500 nM of the forward and reverse
125 primers each and 3 µl of diluted (1:25) cDNA. The thermal profile for the SYBR Green qPCR was 95°C
126 for 8 min, followed by 40 cycles at 95°C for 15 s, 60°C for 15 s and 72°C for 30 s. The mean gene
127 expression was normalized to *Hprt1* and *Rpl32*. In dogs, RNA was extracted from frozen muscle slides
128 using the NucleoSpin RNA extraction kit (Macherey Nagel). RNA was quantified by Nanodrop and the
129 Maxima first strand cDNA master kit (Thermo Fisher) was used to convert 300ng of RNA into
130 cDNA. Gene expression was quantified by real-time qPCR with the QuantStudio™ 3 Real-Time PCR
131 System (Applied Biosystems) using SYBR Green detection kit (Thermo Fisher). The reaction was
132 carried out in triplicates for each sample of diluted (1:10) cDNA. The expression of genes was
133 normalized to *b-actin* gene expression. Results are reported as relative gene expression (2^{-DDCT}).

134 Primers used: Mouse: forward *Ripk3* 5′-CGGGCACACCACAGAACAT-3′, *Ripk3* and reverse 5′-
135 GTAGCACATCCCCAGCACCAC-3′, forward *Ripk1* 5′-AGAAGAAGGGAACTATTCGC-3′ and
136 reverse *Ripk1* 5′-TTCTATGGCCTCCACGAT-3', forward *Bnp* 5'-CAGCTCTTGAAGGACCAAGG-
137 3', reverse 5'-AGACCCAGGCAGAGTCAGAA-3', forward *Myh7* 5'-
138 AGGTGTGCTCTCCAGAATGG-3', reverse 5'-CAGCGGCTTGATCTTGAAGT-3', *Rpl32* - forward
139 5'-TGGTGAAGCCCAAGATCGTC-3', reverse 5'-GGATCTGGCCCTTGAACCTT-3', *Hprt1* -

140 forward 5'-CAGGCCAGACTTTGTTGGAT-3', reverse 5'-TTGCGCTCATCTTAGGCTTT-3'. Rat:
141 forward *Ripk3* 5'-CGTACACGTAGTCCCACTCG-3', reverse 5′- AGGGAGGTGAAGGCTATGGT-
142 3', forward *Ripk1* 5′- GGTCTCCCATGACCCCTTTG-3', reverse 5′-
143 GGTAGGTTGGTCTCAGGCAC-3'. Dog: Forward *Ripk1* 5'-GAATGAGTTCAGCCCTGCTC-3',
144 reverse 5'-CTCGCTCATAGTCGTGGTCA-3', forward *Ripk3* 5'-CAGAGAGGCTCAAGGTCAGG-
145 3', reverse 5'-CGATGTCTGGGCCACTATCT-3' *b-actin* forward 5'-
146 CCATCTACGAGGGGTACGCCC-3' reverse TGCTCGAAGTCC AGGGCGACGTA
147
148 **Histology**
149 Fibrosis was labelled using Epredia Varistain Gemini ES Automated Slide Stainer. For
150 immunofluorescence: rat antibody to CD68 (clone FA-11, 137001, 1/50), rabbit antibody to mouse pan-
151 Laminin (Sigma, L9393, 1/1000), Phospho-RIPK1 (Ser161) antibody (1/100 Invitrogen 105640).
152 Biopsies from GRMD dogs were processed and analysed as previously described[8]. The dried sections
153 were stained for 10 minutes in Hematein and 5 minutes in 1% Eosin, dehydrated in four consecutive
154 baths of ethanol, one bath of xylene and mounted in Canada balsam. One entire section per biopsy was
155 photographed using an AxioObserver Z1 linked to its ICC1 camera (Zeiss), and the MosaiX application
156 of the software AxioVision (Zeiss). The image was then analysed using the software Visilog 6.4
157 (Noesis). A grid of 10 000 mm2 squares was superimposed onto the image of the entire section. At each
158 intercept of the grid (i.e. every 100 mm) the histological aspect of the underlying tissue was manually
159 captioned using predefined annotations. The percentage of each type of histological event was
160 calculated, defined as the percentage of events not corresponding to normal shape fibres. Inflammatory
161 infiltration in dog biopsies was quantified using CD4, CD8, and CD11b immunostainings. 7µm sections
162 from each biopsy were fixed in cold acetone-methanol. After having blocked the endogenous peroxidase
163 activity, the primary antibody (either a rat anti-canine CD4, Serotec H, 1/50, or a rat anti-canine CD8,
164 Serotec H, 1/50, or a mouse anti-canine CD11b, Serotec H, 1/50) was used. The amount of inflammatory
165 cells was normalized to the area of the section[8].
166 Myonecrosis levels in mdx biopsies were determined by measuring the area corresponding to mouse
167 IgG uptake in myofibres (and not in interstitial areas) and expressed as the percentage of the cross-

168 sectional area. Muscle fibre minimal Feret diameter, corresponding to the minimum distance between
169 the two parallel tangents of myofibres, was determined. Images analyses were performed with ImageJ
170 by a specific self-developed macro that recognizes muscle fibres as previously described [9].
171
172 **Cardiac Phenotyping**
173 Mice were trained to be grasped since transthoracic echocardiography (TTE) was performed in
174 conscious, non-sedated mice to avoid any cardiac depressor effect of sedative or anaesthetic agents. Data
175 acquisition was performed every month by a single operator (JT) as previously described [10]. Images
176 were acquired from a parasternal position at the level of the papillary muscles using a 13-MHz linear-
177 array transducer with a digital ultrasound system (Vivid 7, GE Medical System, Horton, Norway). Left
178 ventricular diameters and ejection fraction, anterior and posterior wall thicknesses were serially obtained
179 from M-mode acquisition. Relative LV wall thickness (RWT) was defined as the sum of septal and
180 posterior wall thickness over LV end-diastolic diameter, and LV mass was determined using the
181 uncorrected cube assumption formula (LV mass=$(IVSd+LVIDd+PWTd)^3$-$LVIDd^3$). Peak systolic
182 values of radial SR in the anterior and posterior wall were obtained using Tissue Doppler Imaging (TDI)
183 as previously described [10]. TDI loops were acquired from the same parasternal view at a mean frame
184 rate of 514 fps and a depth of 1 cm. The Nyquist velocity limit was set at 12cm/s. Radial SR analysis
185 was performed offline using the EchoPac Software (GE Medical Systems) by an observer (GD) blinded
186 to the diet of the animals. The Peak systolic of radial SR was computed from a region of interest
187 positioned in the mid anterior wall and was measured over an axial distance of 0.6 mm. The temporal
188 smoothing filters were turned off for all measurements. Because slight respiratory variations exist, we
189 averaged peak systolic of radial SR on 8 consecutive cardiac cycles.

190 Results

191 Firstly, we addressed the relevance of necroptosis in dystrophin deficiency as a potential cell demise
192 involved in locomotor and respiratory muscles and the heart. Because heart or diaphragm muscle
193 biopsies cannot be performed in patients, we aimed at examining tissues in different animal models for
194 DMD. We first investigated degenerating tissues from golden retriever muscular dystrophy (GRMD)

195 dogs that represent a gold standard relevant animal model for DMD[11]. Compared to age-matched wild-
196 type (WT) dogs, 6-month-old-GRMD dogs were characterized by typical high and variable blood
197 creatine kinase levels (p=0.0167) (Figure 1a), assessing a significant ongoing, global myofibre demise.
198 Histological features of myonecrosis in the sartorius and biceps femoris muscles confirmed the presence
199 of recently injured area (Figure 1b). Because myofibre necroptosis comes with an increase of *Ripk3*
200 transcripts in mdx TA muscles, and that RIPK3 upregulation sensitizes muscle cells to TNF-elicited
201 necroptosis[12], we examined whether there was a correlation between muscles presenting high
202 histological necrotic extent and *RIPK3* expression in muscles of GRMD dogs. Sartorius muscles from
203 6- and 12-month-old GRMD dogs were together quantified by qPCR for *RIPK3* transcripts and
204 quantified for evidence of necrotic events and inflammation in hematoxylin & eosin staining.
205 Interestingly, *RIPK3* expression was highly correlated with the extent of myonecrosis (Pearson test,
206 p=0.0076, r=0.8138, n=9 GRMD muscles) (Figure 1b), but not with the inflammatory area (p=0.1409)
207 (Figure 1c), suggesting that *RIPK3* elevation is specific to necrotic demise, rather than post-necrotic
208 events such as myeloid infiltrate. Similarly, *RIPK3* transcripts increased in the GRMD diaphragm
209 compared to age-matched WT dogs, and *RIPK3* expression was also positively correlated with *RIPK3*
210 expression in these muscles (p=0.0307) (Figure 1d-f). Thus, RIPK3-dependant cell death does not only
211 involve ambulatory, but also the main respiratory musculature in the DMD pathogenic course. In the
212 heart, whilst we observed no significant increase in the necrosome transcripts in the left ventricle of 6-
213 month-old GRMD dogs (Figure 1g,h), we found a dramatic increase of immunoreactivity of GRMD
214 dog's cardiomyocytes to antibodies directed against phospho-RIPK1 (Ser161), indicating that RIPK1 is
215 primed for either extrinsic apoptosis or canonical necroptosis (Figure 1i)[13,14].
216 Thus, to determine whether necroptosis has a functional role in progressive cardiomyopathy or in
217 myonecrosis affecting the diaphragm of dystrophin-deficient mice, we generated mdx*Ripk3*$^{-/-}$ mice by
218 crossing mdx with *Ripk*3-KO mice, which compromise dystrophic mice for RIPK3-dependent
219 necroptosis[15]. Mdx*Ripk3*$^{+/+}$ (hereafter named mdx*Ripk3*$^{+/+}$ or mdx) and mdx*Ripk3*$^{-/-}$ littermates were
220 kept for ageing to reach the maximum mdx pathogenic state in striated muscles. We first examined
221 whether the long-term genetic inhibition of necroptosis would promote sarcopenia by repressing MuSCs
222 density and the regenerative capacity of skeletal muscle. Indeed, a recent article indicated that

223 necroptosis inhibition generates a MuSCs depletion by inducing the death of PAX7-positive cells, with
224 a subsequent deficit in myogenesis associated with a dramatically reduced muscle strength in adult mdx
225 mice [6]. In biceps from 18-month-old mdx*Ripk3*$^{-/-}$ mice, *Ripk1* transcripts were downregulated compared
226 to *Ripk3*$^{+/+}$ littermates (Figure 2a), indicating that canonical necroptosis is repressed in mdx*Ripk3*$^{-/-}$
227 mice. To determine whether the defect of necroptosis signalling compromises muscle function, mdx and
228 mdx*Ripk3*$^{-/-}$ littermates underwent forced treadmill exercise with progressive increase of speed, until
229 exhaustion. Control mdx mice were characterized by an important variability in running performance,
230 expressed in the running distance (Figure 2b) or the maximum aerobic speed before exhaustion
231 (Figure 2c). mdx*Ripk3*$^{-/-}$ mice showed more homogenous capacities (coefficient of variation:
232 mdx: 20,99% *versus* mdx*Ripk3*$^{-/-}$ 12.66%). On average, mdx*Ripk3*$^{-/-}$ ran ~ 10% longer than mdx
233 littermates, despite no statistical difference likely due to the variability of the control mdx phenotype
234 (p=0.5530). The putative atrophy of *Ripk3*-/- dystrophic muscles was examined using muscle mass
235 normalized to the individual size of the animals, assessed by the tibial length (TL). TA, EDL and biceps
236 muscle mass remained unchanged in aged mdx*Ripk3*$^{-/-}$ compared to mdx*Ripk3*$^{+/+}$ mice (Figure 2d).
237 Although young mdx muscles show extensive necrotic events leading to the accumulation of fibrotic
238 tissue, muscles from old mice are typically spared. In the rare post-necrotic areas in TAs from old mdx
239 and mdx*Ripk3*$^{-/-}$ mice, we found an equal density of Ki67-positive cells (Figure 2e,f), suggesting that
240 necroptosis inhibition does not affect MuSC proliferation in mdx muscle at this age. The mean of pooled
241 minimum Feret of TA myofibres (Figure 2g), as well as the relative distribution of myofibre size (Figure
242 2h), were strictly unchanged. Interestingly, we found that RIPK3 depletion reduced fibrosis in the TA
243 (p=0.0252) (Figure 2i), suggesting a cumulative cytoprotective effect regarding ancient degenerative
244 events. To further examine any possible evidence of regenerative default in mdx*Ripk3*$^{-/-}$ muscles, we
245 analysed biceps muscles for *Pax7* (Figure 2j) and *myogenin* (Figure 2k) expression but observed no
246 difference. Of note, we found a significant downregulation of *myostatin* expression (p=0.0082), a
247 biomarker of neuromuscular disorders while *follistatin* was not significantly repressed (p=0.4452)
248 (Figure 2l,m).
249 We then examined whether the pathogenic features of the mdx diaphragm are improved by RIPK3
250 depletion (Figure 3). In histology, the localization of blood proteins such as albumin or immunoglobulins

251 within sarcoplasm is a reliable marker for the necrotic fate of myofibre[16,17]. Muscles from eighteen-
252 month-old mice showed IgG immunoreactivity almost only localized at the extracellular compartment
253 (Figure 3a), and rarely within myofibres, indicating no/little ongoing myonecrosis. No difference was
254 found in both genotypes (unpaired t-test, p=0.1914). The density of myofibres with leaky sarcolemma
255 was extremely low in both genotypes (2.3 fibres/mm^2 in mdx versus 2.6 fibres/mm^2 in mdx*Ripk3*$^{-/-}$)
256 (Figure 3b,c). This was neither associated with high-density cell pockets (Figure 3d) nor with CD68-
257 positive cell infiltrates (Figure 3e). Furthermore, only a low percentage of centrally nucleated fibres was
258 found in the mdx diaphragm (5-10% of myofibres) (Figure 3f). These observations suggested that the
259 diaphragm from 18-month-old mdx mice stand at relative homeostasis with little/no ongoing
260 myonecrosis, regardless of RIPK3 expression. Examining the profile of myofibre size, we observed a
261 moderate decrease of myofibre size in mdx*Ripk3*$^{-/-}$ diaphragm compared to mdx littermates (16.6 in mdx
262 versus 16.1 in mdx*Ripk3*$^{-/-}$, p<0.0001, Mann Whitney test, n>16,000 myofibres in each group, included
263 in six mdx muscles, and eight mdx*Ripk3*$^{-/-}$ muscles). Dystrophin-deficient muscles are characterized by
264 an increased heterogeneity in myofibre size, illustrated by an increase of the variance coefficient[18].
265 RIPK3-deficiency decreased the mean-variance coefficient of myofibres in mdx mice (Figure 3i,
266 unpaired t-test p=0.0431). Fibrosis deposition in respiratory muscles, such as the diaphragm, is a key
267 pathogenic event in DMD pathogenesis and correlates with a bad prognosis in patients. To determine
268 whether RIPK3 also mediates fibrosis deposition in the diaphragm, muscle sections were stained with
269 Sirius red (Figure 3k), and we observed less collagen deposition in mdx*Ripk3*$^{-/-}$diaphragms compared to
270 mdx littermates (Figure 3k, unpaired t-test, p=0.0414). Together, our data demonstrate that RIPK3
271 participates in diaphragm pathogenesis in mdx mice by promoting interstitial fibrosis.
272 We next addressed the role of necroptosis in the development of cardiomyopathy upon dystrophin
273 deficiency. Importantly, end-stage cardiomyopathy is a major concern in the survival of boys and is
274 associated with hallmarks of cardiomyoblast necrosis and fibrosis deposition. In GRMD dogs, RIPK1
275 was found phosphorylated at the Ser161 site in the heart (Figure 1i), indicating an early step of activation
276 of RIPK1-dependant apoptosis or necroptosis[14]. Similar p-RIPK1 immunoreactivity to GRMD dogs was
277 observed in the hearts of R-DMDdel52 rats (Figure 4a) that develop an early cardiomyopathy[19].
278 Dystrophin-deficient rats also had a significant increase of *Ripk1* (p=0.0070, t-test) and *Ripk3*

279 (p=0.0080, t-test) transcripts in heart tissue compared to WT rats (Figure 4b,c), suggesting advanced
280 necroptosis activation in the heart from R-DMDdel52 rats. This contrasted with dogs that displayed no
281 significant elevation of *RIPK1* and *RIPK3* transcription (Figure 1g,h), in agreement with rare fresh
282 necrotic events observed in dystrophic hearts of GRMD dogs. To determine the role of necroptosis in
283 the progressive cardiomyopathy of dystrophin-deficient hearts, we analysed the heart phenotype of 18-
284 month-old mdx*Ripk3*$^{-/-}$ mice (Figure 4 d-k). RIPK3 depletion decreased cardiac compensatory
285 hypertrophy in mdx mice (Figure 4d,e). At the investigated age, we found no significant levels of
286 ongoing degeneration in the heart, displaying little CD68-positive cell infiltration whatever the genotype
287 (Figure 3f), which suggested an accumulation of past degenerative events with little evolution over time
288 at this age. Interstitial collagen deposition was reduced by almost 50% in the right ventricle of mdx*Ripk3*$^{-}$
289 $^{/-}$ mice compared to their mdx control littermates (Figure 4h,g). Furthermore, the hearts of mdx*Ripk3*$^{-/-}$
290 mice showed significantly reduced levels of *Bnp* and *Myf7* transcripts, two sensitive markers of cardiac
291 hypertrophy (Figure 4i,j).
292 We thus examined whether the improvement of the deleterious phenotype of cardiomyopathy conferred
293 by RIPK3 depletion was validated at the 2D and functional levels and quantified routine
294 echocardiographic parameters using the M(otion)-mode (Figure 5). Compared to wild-type mice, aged
295 mdx mice are generally characterized by eccentric hypertrophy characterized by a transiently increased
296 LV mass with increased left ventricle (LV) end-diastolic and end-systolic diameter. This is followed by
297 a decompensated dilated cardiomyopathy associated with a reduction in LV fractional shortening and a
298 decreased LV mass[20]. We confirmed that our 18-month-old mdx mice suffered from eccentric
299 hypertrophy with an increased LV mass, associated with a reduced LV internal diameter in diastole
300 (LVIDd) and systole (LVIDs) (Figure 5a-4c and Supplementary Table 1). Of note, compared to mdx
301 mice, mdx*Ripk3*$^{-/-}$ littermates displayed a 30% reduction of the LV mass linked to a decrease in LVIDd
302 that contributed to the restoration of the LV relative wall thickness value (Figure 5d), and unchanged
303 fractional shortening of the LV, strain rate of cardiomyocytes from the anterior wall (Figures 5e, f) and
304 heart rate (Supplementary Table 1). Altogether, these data suggested that in the mdx model, RIPK3-
305 dependent necroptosis participates in the long-term development of cardiac hypertrophy and dysfunction

306 and that in these conditions, RIPK3 deficiency has overall cytoprotective effects against dystrophic-
307 associated cardiac deleterious phenotype in the mouse.
308

309 **Discussion**

310 Necroptosis is now considered a new therapeutic target for several degenerating disorders, including
311 cardiovascular neurodegenerative, and autoimmune diseases[21]. Dystrophin absence and DUX4
312 overexpression can lead to myofibre necroptosis *in vivo*[12]. Translating these discoveries into the clinic
313 for neuromuscular disorders requires an understanding of 1-the long-term consequences of necroptosis
314 inhibition in dystrophic conditions and 2-the role of necroptosis in the DMD cardiorespiratory
315 phenotype.
316 While locomotor tissues can be harvested in DMD patients for diagnostic purposes and could be used
317 for research purposes, respiratory or heart biopsies were not available. We then used dystrophic dogs
318 and rats which are highly relevant animal models for DMD and reproduce the main aspects of DMD
319 pathogenesis[11]. RIPK3 overexpression is a biomarker for myofibre necroptosis in mdx mice, and
320 sensitizes myoblasts to TNF-elicited necroptosis[5]. Using sartorius and femoral biceps, diaphragm and
321 cardiac tissues from 6-month-old GRMD dogs, we first assessed different levels of activation of the
322 early steps of the RIPK1-RIPK3 canonical necroptotic pathway. RIPK3 upregulation in limb muscles,
323 and diaphragm, and its correlation with the myonecrosis extent (Figure 1b), suggest a role for RIPK3 in
324 the myonecrosis affecting GRMD dogs, especially in cells expressing p-RIPK1, which prime cells to
325 programmed necrosis[14]. RIPK3 typically recruits MLKL during final necroptosis induction, and p-
326 MLKL causes membrane permeability and necrotic morphology. Interestingly, dogs and other species
327 belonging to the *Carnivora* order express crucial proteins required for necroptosis activation such as
328 RIPK1, RIPK3, DNA-dependant activator of interferon regulatory factors (DAI) and TIR-domain-
329 containing adaptor-inducing IFNβ (TRIF), however, they do not express MLK[23]. The molecular
330 mechanisms of cell death execution in RIPK3-dependant but MLKL-independent necrosis, involvement
331 remains an open question.
332 Notably, necrotic demise affecting the diaphragm and heart are key events leading to the short life
333 expectancy of DMD boys. Herein, we provide evidence that beyond its role in the degeneration of

334 locomotor muscles, necroptosis also takes part in the respiratory and cardiac phenotypes in the mdx
335 model of DMD, notably by promoting tissue fibrosis. Accumulation of extracellular matrix deposition
336 following myonecrosis is a central pathogenic process responsible for the loss of function of dystrophic
337 muscles, by progressively replacing functional muscle tissue in both the myocardium and skeletal
338 muscles[2]. Therefore, understanding the molecular pathways directly or indirectly leading to myofibre or
339 cardiomyocyte death or fibrosis is highly relevant.
340 In dystrophin-deficient mice, investigating the phenotypes of the diaphragm and heart requires the
341 generation of dystrophic and necroptosis-incompetent mice that would reach sufficient age to
342 progressively develop a significant phenotype[24,25]. Compared to young dystrophic TA, the diaphragm
343 from 18-month-old mdx mice showed IgG immunoreactivity mainly trapped in the large fibrotic area
344 (Figure 3a) and barely detected within the myofibre compartment (Figure 3c), suggesting little/no
345 ongoing myonecrosis. The observed low percentage of central nucleation together with low cell
346 infiltration and high fibrosis indicates that this phenotype is the outcome of accumulating necrotic and
347 regenerative events over time. Fibrosis decrease was observed in the diaphragm and was associated with
348 a decrease in the mean myofibres size and size variability (Figure 3g-k). These results are consistent
349 with a previous report assessing significant myofibre cytoprotection in the diaphragm[26]. We also found
350 a significant reduction of fibrosis in the TA of old mdx*Ripk3*$^{-/-}$ (Figure 2m) compared to mdx littermates,
351 suggesting that the effects of necroptosis inhibition on muscle histology benefit both locomotor and
352 respiratory muscles.
353 Two recent studies reported that necroptosis is involved in post-lesional myogenesis[6,27]. However, the
354 underlying mechanisms of action of necroptosis on regeneration seem unclear: Sreenivasan and
355 colleagues observed exclusive expression of RIPK3 in mdx MuSCs and not in myofibres. MuSCs
356 depleted for RIPK3 led to a dramatic loss of PAX7-expressing cells and severely impaired muscle
357 function[6]. On another hand, Zhou and colleagues found that myofibres express RIPK3 and MLKL and
358 are susceptible to necroptotic demise. They demonstrated that myofibre necroptosis indirectly modulates
359 muscle regeneration by releasing Tenascine-C, which is required for MuSCs proliferation. An effect of
360 myofibre necroptosis on *Pax7* expression and myofibre size was observed *in vivo* at 7 and 15 days post-
361 injury[27]. As the full effects on regeneration are generally observed at a later stage, after 4 weeks post-

362 injury, it is unclear in this study whether the depletion of necroptosis irreversibly stops myogenesis or
363 only delays it.
364 Herein, we found no impairment of running performance in dystrophic *Ripk3*$^{-/-}$ mice, and no/little effect
365 on muscle weight, while confirming the downregulation of *Ripk1* in muscle extracts. The weight of limb
366 muscles was unchanged, as myofibre size (Figure 2a-h). *Pax7* and *myogenin* expression were not
367 reduced in mdxRipk3-/-mice, suggesting there is no depletion of MuSCs. Together, our results
368 demonstrate that in mdx mice, a long-term necroptosis inhibition does not lead to sarcopenia of
369 dystrophic muscle, but rather has beneficial effects since it dampens fibrosis. The lack of observed
370 sarcopenia in our mdx*Ripk3*$^{-/-}$ dystrophic mice could for instance be explained by a delay of myogenesis
371 when necroptosis is prevented. Indeed, slowing down the kinetics of differentiation does not necessarily
372 impair regeneration[28]. It is also possible that any effect, positive or negative of RIPK3-deficiency on
373 regeneration could be mitigated by the cytoprotective effects of necroptosis inhibition. Not to be
374 forgotten that the regenerative process remains a consequence of previous degenerative events. Hence,
375 the less degeneration, the less resulting regeneration. Therefore, any protection against myonecrosis is
376 expected to hide any putative default on regeneration.
377 In mdx mice, myofibre necrosis does not lead to a dramatic lack of function of the limb, respiratory or
378 cardiac muscles[29]. On another hand, pathology is dramatically exacerbated in R-DMDdel52 rats with a
379 reduced life expectancy and cardiomyopathy functionally assessed in young adults[19]. Phospho-Ser161
380 RIPK1 is strongly upregulated in nuclei from cardiomyocytes, and the RIPK1/3 axis is largely
381 overexpressed, suggesting ongoing necroptosis activation. In mdx mice, the heart pathogenic phenotype
382 becomes detectable using M-mode echocardiography only after 10-12 months of age compared to wild-
383 type mice. Heart weight, histological features, and analysis can discriminate healthy from dystrophic
384 aged hearts[25,30,31]. Necroptosis depletion reduced heart weight, and biomarkers of hypertrophic
385 cardiomyopathy such as *Bnp* and *Myh7* transcripts[32,33] and fibrosis (Figures 4). BNP is upregulated in
386 mdx compared to C57BL/10 control mice and restored to baseline in mdx mice treated by rAAV9-
387 mediated microdystrophin[34]. The RIPK1/3 axis may therefore represent an interesting therapeutic target
388 to counteract the development of cardiomyopathy in DMD. The role of canonical necroptosis has been
389 found in cardiovascular diseases, such as atherosclerosis, ischemia-reperfusion injuries, myocardial

390 infarction, myocarditis and chemically-induced cardiomyopathy[35]. We failed to observe a significant
391 decrease in cardiomyocyte demise and necroinflammation. This is likely due to rare cell death events
392 affecting the cardiomyocytes of mdx mice at this age. Indeed, only a minority of mdx hearts showed
393 ongoing active necroinflammation area (Figure 4f). However, a reduction of cardiac hypertrophy linked
394 with a reduction of fibrosis deposition suggests, over time, less accumulation of myocardial cell death
395 susceptible to be replaced by collagen and overall improved tissue homeostasis.
396
397 In conclusion, using dogs, rats and mice models of DMD pathogenesis, we found that RIPK3 participates
398 in the pathogenesis of mdx mice at different levels, mediating necrosis and fibrosis accumulation in
399 locomotor, respiratory, and cardiac muscles without evidence of a detrimental effect on skeletal muscle
400 regeneration. This study, therefore, suggests that necroptosis prevention can be beneficial both to
401 skeletal muscle and heart phenotype in DMD conditions and paves the way for considering necroptosis
402 as a promising therapeutic target for DMD.

Acknowledgements

We thank Dr V. M. Dixit for *Ripk3* knockout mice. We also thank J. Ternacle, B. Drayton Libotte, L. Guillaud and X. Decrouy for technical assistance and C. Laisne and D. Gelperowic for taking good care of animals, and the VOUSH group for fruitful discussions. This work was supported by the Association Française contre les Myopathies (AFM-Téléthon) through the Translamuscle I (#19507) and Translamuscle II (#22946) programs.

Conflict of Interest

The authors declare no conflict of interest

Bibliography

1. Relaix, F. *et al.* Perspectives on skeletal muscle stem cells. *Nat Commun* **12**, 692 (2021).
2. Desguerre, I. *et al.* Endomysial fibrosis in Duchenne muscular dystrophy: a marker of poor outcome associated with macrophage alternative activation. *J Neuropathol Exp Neurol* **68**, 762–773 (2009).
3. Khirani, S. *et al.* Respiratory muscle decline in Duchenne muscular dystrophy. *Pediatr Pulmonol* **49**, 473–481 (2014).
4. Fayssoil, A., Abasse, S. & Silverston, K. Cardiac Involvement Classification and Therapeutic Management in Patients with Duchenne Muscular Dystrophy. *J Neuromuscul Dis* **4**, 17–23 (2017).
5. Morgan, J. E. *et al.* Necroptosis mediates myofibre death in dystrophin-deficient mice. *Nat Commun* **9**, 3655 (2018).
6. Sreenivasan, K. *et al.* Attenuated Epigenetic Suppression of Muscle Stem Cell Necroptosis Is Required for Efficient Regeneration of Dystrophic Muscles. *Cell Rep* **31**, 107652 (2020).
7. Zhou, S. *et al.* Myofiber necroptosis promotes muscle stem cell proliferation via releasing Tenascin-C during regeneration. *Cell Res* **30**, 1063–1077 (2020).
8. Barthélémy, I. *et al.* Effects of an Immunosuppressive Treatment in the GRMD Dog Model of Duchenne Muscular Dystrophy. *PLoS ONE* **7**, e48478 (2012).
9. Reyes-Fernandez, P. C., Periou, B., Decrouy, X., Relaix, F. & Authier, F. J. Automated image-analysis method for the quantification of fiber morphometry and fiber type population in human skeletal muscle. *Skelet Muscle* **9**, 15 (2019).
10. Czibik, G. *et al.* Dysregulated Phenylalanine Catabolism Plays a Key Role in the Trajectory of Cardiac Aging. *Circulation* **144**, 559–574 (2021).
11. Wells, D. J. Tracking progress: an update on animal models for Duchenne muscular dystrophy. *Disease Models & Mechanisms* **11**, dmm035774 (2018).
12. Morgan, J. E. *et al.* Necroptosis mediates myofibre death in dystrophin-deficient mice. *Nat Commun* **9**, 3655 (2018).

440 13. McQuade, T., Cho, Y. & Chan, F. K.-M. Positive and Negative Phosphorylation Regulates
441 RIP1 and RIP3-Induced Programmed Necrosis. *Biochem J* **456**, 409–415 (2013).
442 14. Zhang, Y. *et al.* RIP1 autophosphorylation is promoted by mitochondrial ROS and is essential
443 for RIP3 recruitment into necrosome. *Nat Commun* **8**, 14329 (2017).
444 15. Newton, K., Sun, X. & Dixit, V. M. Kinase RIP3 is dispensable for normal NF-kappa Bs,
445 signaling by the B-cell and T-cell receptors, tumor necrosis factor receptor 1, and Toll-like receptors 2
446 and 4. *Mol Cell Biol* **24**, 1464–1469 (2004).
447 16. Straub, V., Rafael, J. A., Chamberlain, J. S. & Campbell, K. P. Animal Models for Muscular
448 Dystrophy Show Different Patterns of Sarcolemmal Disruption. *J Cell Biol* **139**, 375–385 (1997).
449 17. Bencze, M., Periou, B., Baba-Amer, Y. & Authier, F. J. Immunolabelling Myofiber
450 Degeneration in Muscle Biopsies. *JoVE (Journal of Visualized Experiments)* e59754 (2019)
451 doi:10.3791/59754.
452 18. Briguet, A., Courdier-Fruh, I., Foster, M., Meier, T. & Magyar, J. P. Histological parameters
453 for the quantitative assessment of muscular dystrophy in the mdx-mouse. *Neuromuscul Disord* **14**,
454 675–682 (2004).
455 19. Taglietti, V. *et al.* Duchenne muscular dystrophy trajectory in R-DMDdel52 preclinical rat
456 model identifies COMP as biomarker of fibrosis. *Acta Neuropathologica Communications* **10**, 60
457 (2022).
458 20. Quinlan, J. G. *et al.* Evolution of the mdx mouse cardiomyopathy: physiological and
459 morphological findings. *Neuromuscul Disord* **14**, 491–496 (2004).
460 21. Choi, M. E., Price, D. R., Ryter, S. W. & Choi, A. M. K. Necroptosis: a crucial pathogenic
461 mediator of human disease. *JCI Insight* **4**, e128834 (2021).
462 22. Mariot, V. *et al.* RIPK3-mediated cell death is involved in DUX4-mediated toxicity in
463 facioscapulohumeral dystrophy. *J Cachexia Sarcopenia Muscle* (2021) doi:10.1002/jcsm.12813.
464 23. Dondelinger, Y., Hulpiau, P., Saeys, Y., Bertrand, M. J. M. & Vandenabeele, P. An
465 evolutionary perspective on the necroptotic pathway. *Trends in Cell Biology* **26**, 721–732 (2016).
466 24. Stedman, H. H. *et al.* The mdx mouse diaphragm reproduces the degenerative changes of
467 Duchenne muscular dystrophy. *Nature* **352**, 536–539 (1991).
468 25. Quinlan, J. G. *et al.* Evolution of the mdx mouse cardiomyopathy: physiological and
469 morphological findings. *Neuromuscul Disord* **14**, 491–496 (2004).
470 26. Stupka, N., Schertzer, J. D., Bassel-Duby, R., Olson, E. N. & Lynch, G. S. Stimulation of
471 calcineurin Aα activity attenuates muscle pathophysiology in mdx dystrophic mice. *American Journal*
472 *of Physiology-Regulatory, Integrative and Comparative Physiology* **294**, R983–R992 (2008).
473 27. Zhou, S. *et al.* Myofiber necroptosis promotes muscle stem cell proliferation via releasing
474 Tenascin-C during regeneration. *Cell Res* **30**, 1063–1077 (2020).
475 28. Bencze, M. *et al.* Proinflammatory Macrophages Enhance the Regenerative Capacity of
476 Human Myoblasts by Modifying Their Kinetics of Proliferation and Differentiation. *Molecular*
477 *Therapy* **20**, 2168–2179 (2012).
478 29. Partridge, T. A. The mdx mouse model as a surrogate for Duchenne muscular dystrophy. *The*
479 *FEBS Journal* **280**, 4177–4186 (2013).
480 30. Zhang, W. *et al.* Abnormal cardiac morphology, function and energy metabolism in the
481 dystrophic mdx mouse: An MRI and MRS study. *Journal of Molecular and Cellular Cardiology* **45**,
482 754–760 (2008).
483 31. Li, W., Liu, W., Zhong, J. & Yu, X. Early manifestation of alteration in cardiac function in
484 dystrophin deficient mdx mouse using 3D CMR tagging. *J Cardiovasc Magn Reson* **11**, 40 (2009).
485 32. Hasegawa, K. *et al.* Ventricular expression of brain natriuretic peptide in hypertrophic
486 cardiomyopathy. *Circulation* **88**, 372–380 (1993).
487 33. Fananapazir, L., Dalakas, M. C., Cyran, F., Cohn, G. & Epstein, N. D. Missense mutations in
488 the beta-myosin heavy-chain gene cause central core disease in hypertrophic cardiomyopathy. *PNAS*
489 **90**, 3993–3997 (1993).
490 34. Shin, J.-H. *et al.* Improvement of cardiac fibrosis in dystrophic mice by rAAV9-mediated
491 microdystrophin transduction. *Gene Ther* **18**, 910–919 (2011).
492 35. Zhe-Wei, S., Li-Sha, G. & Yue-Chun, L. The Role of Necroptosis in Cardiovascular Disease.
493 *Front Pharmacol* **9**, 721 (2018).

494 **Figures Bencze et al. 2022**

495

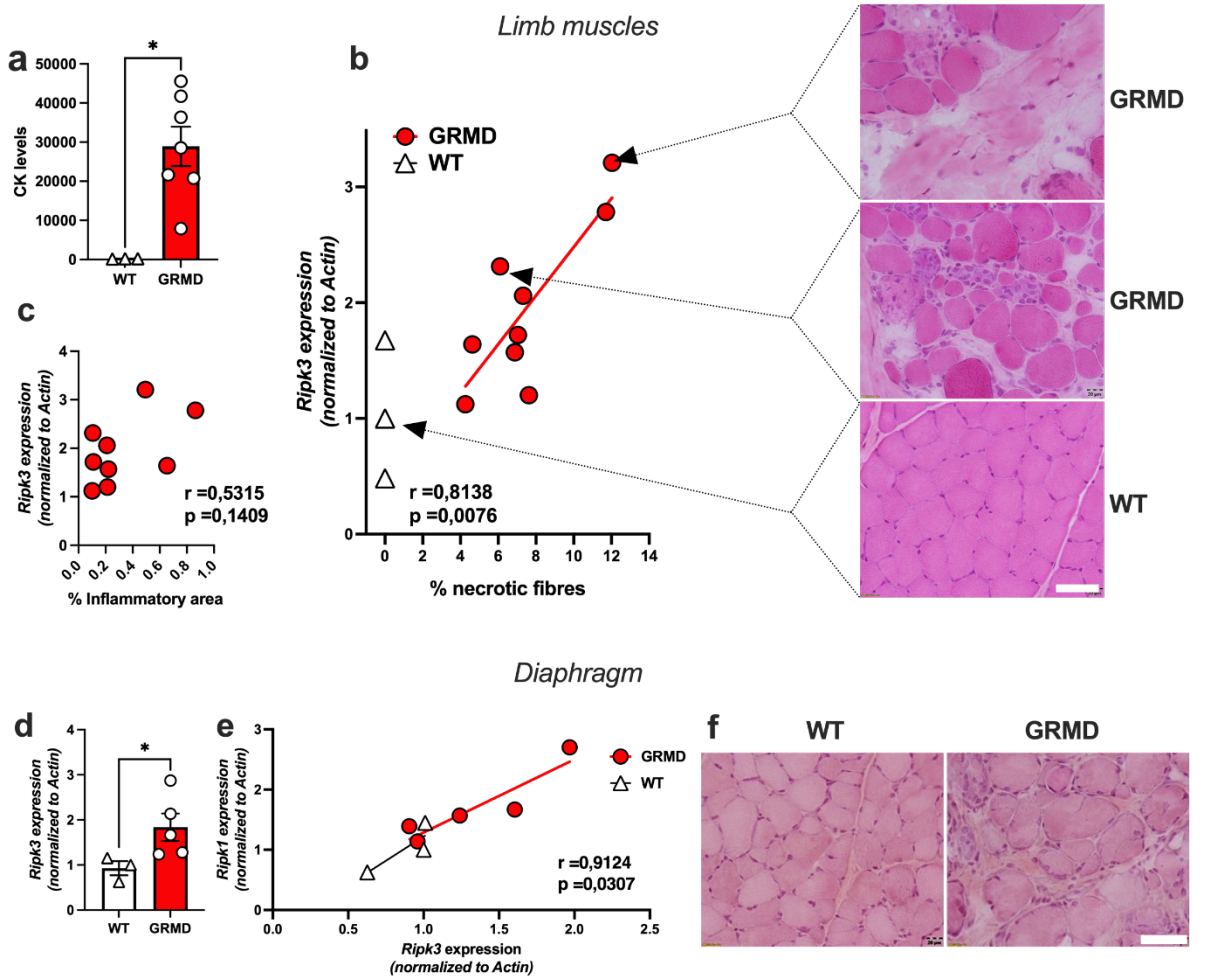

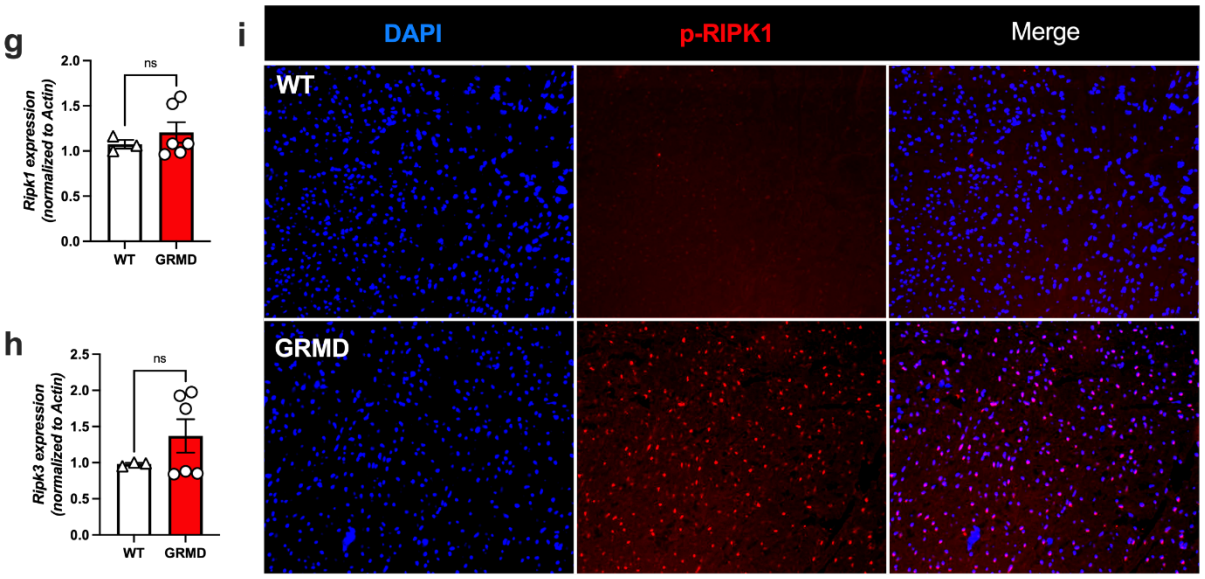

496

Figure 1: The RIPK1-RIPK3 axis is dysregulated in the skeletal muscles and the heart of dystrophic dogs.

(a) Quantification of serum CK in six-month-old WT and GRMD dogs. (b) Pearson correlation coefficient (r) and p-value (p) between necrotic fibre percentage and *RIPK3* transcripts expression normalized to *ACTIN*. Representative H&E staining of the sartorius muscle corresponding to related biopsied muscle. Scale bar: 20 µm. (d) Pearson correlation coefficient and p-value between the percentage of inflammation and *RIPK3* transcripts expression. (d) Quantification of *RIPK3* expression in the diaphragms of 6-month-old WT and GRMD dogs. (e) Pearson correlation between *RIPK1* and *RIPK3* expression in the diaphragm. (f) H&E staining of the diaphragm muscle. (g) In the heart left ventricle of GRMD and WT dogs, quantification of *RIPK1* and (h) *RIPK3* transcripts normalized to *ACTIN*. (i) Representative image of a left ventricle heart from WT and GRMD dogs labelled with an antibody directed against the phosphorylated form of RIPK1 (S161). Data are given as means ± s.e.m. Ns: Not significant, *: p-value < 0.05.

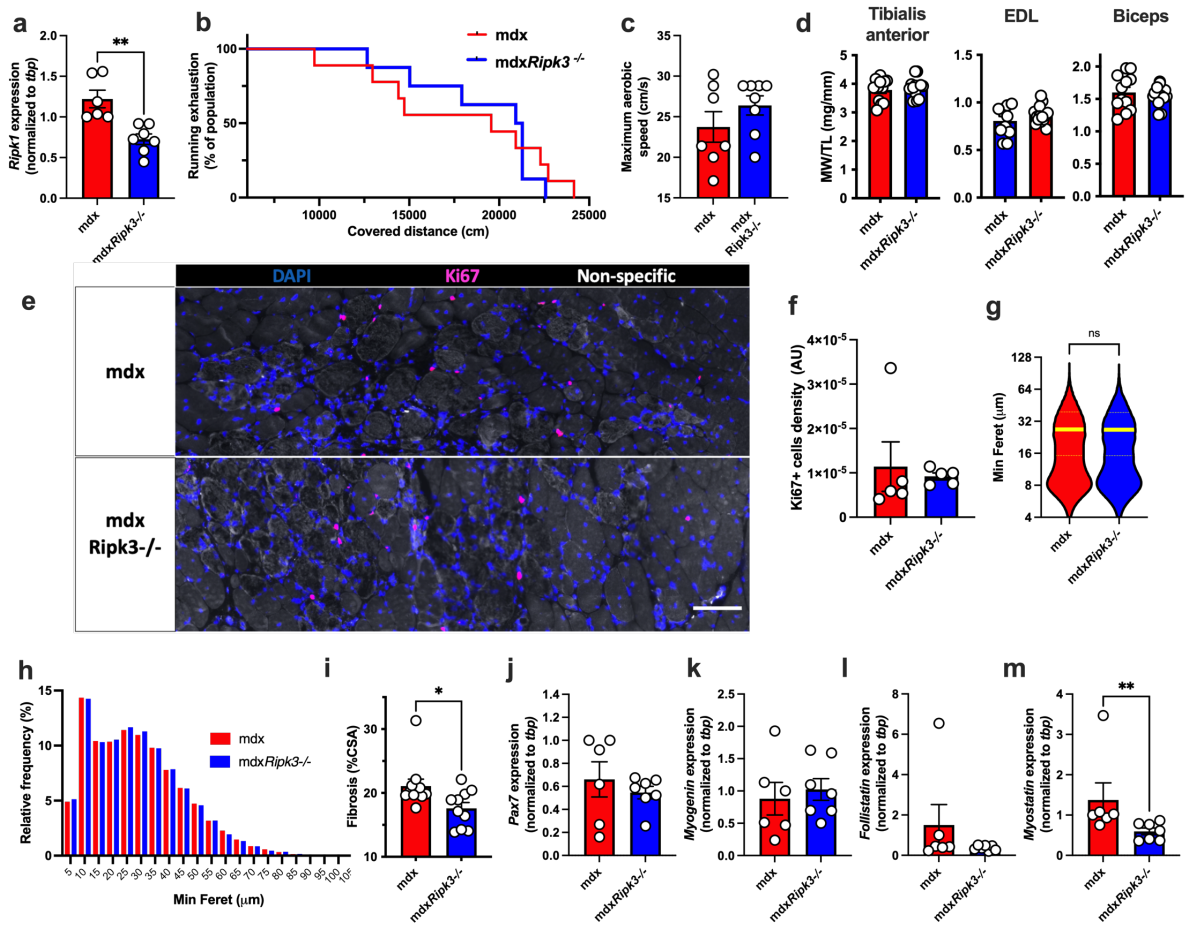

Figure 2. The genetic ablation of RIPK3 does not promote sarcopenia in 18-month-old mdx mice.

Quantification of *Ripk1* transcripts in the eighteen-month-old biceps muscles (a) Seventeen-month-old mdx*Ripk3*+/+ (i.e. mdx) and mdx*Ripk3*-/- male mice were submitted to forced treadmill running with a progressive increase of speed. (b) Endurance curve of running mice against covered distance expressed in cm. (c) Maximum aerobic speed before mice exhaustion. Data are given as means ± s.e.m. mdx*Ripk3*+/+, n=7, mdx*Ripk3*-/-, n=8. Shapiro-Wilk test followed by a Mann-Whitney test. (d) Tibialis anterior (TA), EDL and biceps muscles were harvested, and muscle weight (MW) was determined (and normalized to tibial length (MW/TL). (e) TA immunolabeling using antibodies directed against Ki67 (red). (f) Quantification of the density of Ki67-positive cells. (g) Violin plot of the pooled minimum Feret of TA myofibres (mdx: n=33,142 myofibres out of 7 distinct muscles; mdx*Ripk3*-/-, n=26,469 myofibres out of 9 distinct muscles, Mann-Whitney test p=0.1526). (h) Relative frequencies of minimum Feret from TA myofibres are expressed in percentage. (i) Quantification of collagen deposition using Sirius red dye. The normal distribution of data was tested using the Kolmogorov-

Smirnov test (passing normality test with α=0.05), leading to either t-tests or Mann-Whitney tests. (j) Quantification of the transcript levels of *Pax7*, (k), *myogenin*, (l) *follistatin* and (m) *myostatin* in the biceps, by quantitative PCR. Data are given as means ± s.e.m. Ns: Not significant, *: p-value < 0.05, **: p-value < 0.01. Scale bar:100 µm

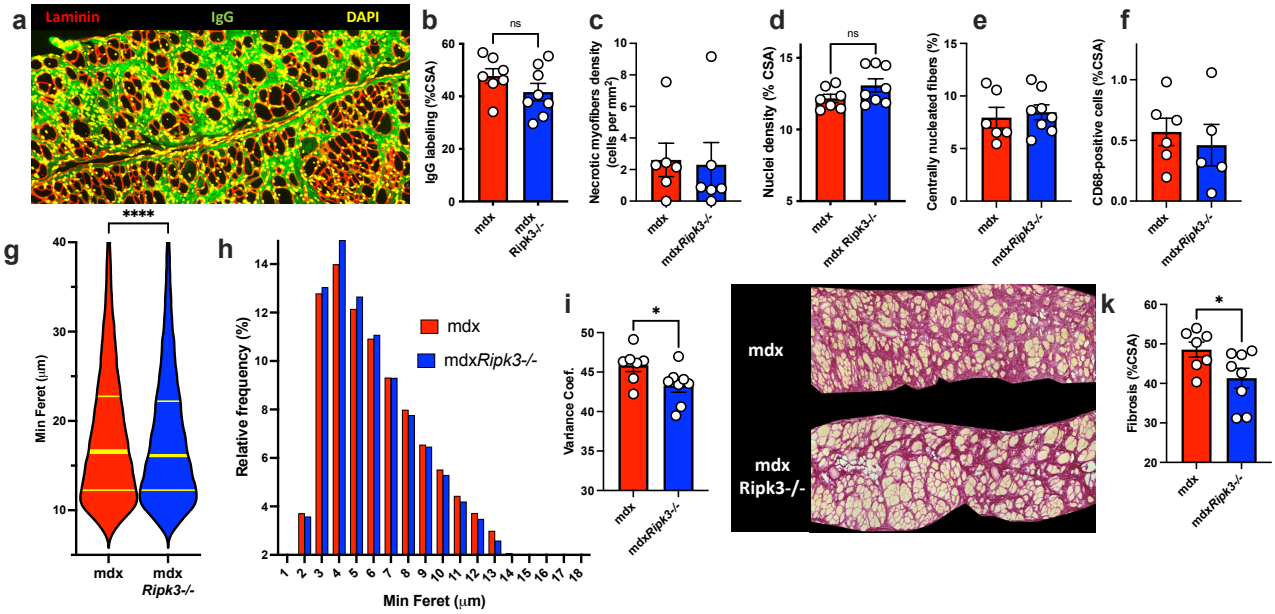

Figure 3: Necroptosis participates in the diaphragm fibrosis in mdx mice.

(a) Representative image of IgG uptake in diaphragms of 18-month-old mdx (mdx*Ripk3*$^{+/+}$) and mdx*Ripk3*$^{-/-}$ mice. (b) Quantification of IgG uptake labelling expressed in percentage of cross-sectional area (%CSA). (c) Quantification of myonecrosis extent. Myonecrosis is defined as the area occupied by leaky myofibres (i.e immunoreactive for mouse IgG uptake). Quantification of nuclear density expressed as a percentage of CSA (d), CD68-positive macrophage infiltrates expressed in percentage of CSA (e), and centrally nucleated myofibres expressed as a percentage of myofibres (f). (g) Violin plot of the minimum Ferets of diaphragm myofibres. (mdx, n=16873 including 7 distinct muscles, mean:18,61 ± 0.06555; mdx*Ripk3*-/-, n=31666 including 8 distinct muscles, mean:18,21 ± 0.04554, two-tailed Mann-Whitney test p < 0,0001). (h) Relative frequency of minimum Ferets from diaphragm myofibres. Data are expressed as a percentage. (i) Quantification of the variance coefficient of the minimum Feret of myofibres, (j) representative picture of Sirius red staining (k) Quantification of diaphragm fibrosis. The normal distribution of data was tested using the Kolmogorov-

545 Smirnov test (passing normality test with α=0.05), leading to either t-tests or Mann-Whitney tests. Data
546 are given as means ± s.e.m. Ns: Not significant, *: p-value < 0.05, ****: p-value < 0.0001.

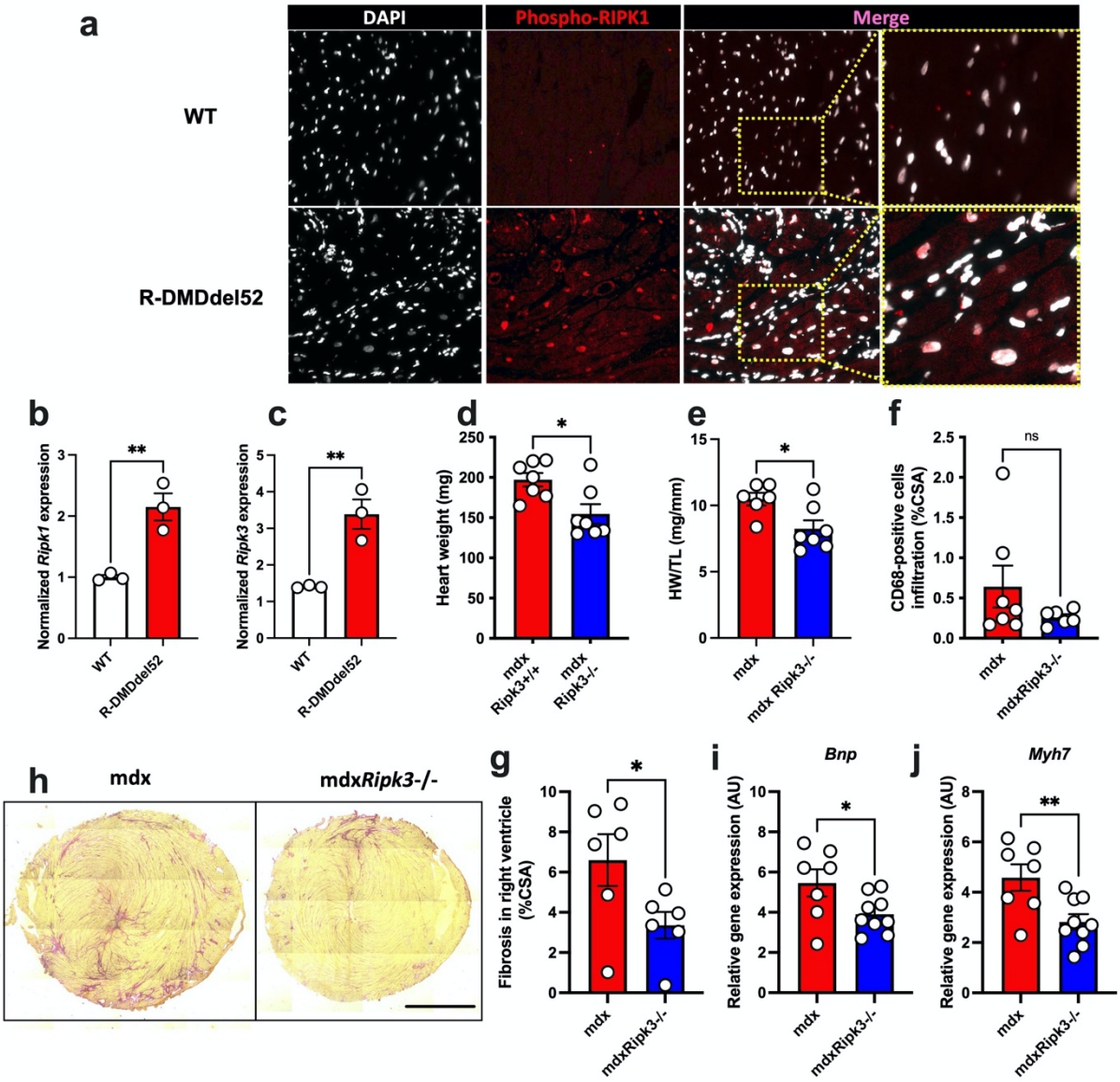

547

548 **Figure 4: RIPK3 mediates the compensatory hypertrophy of the dystrophin-deficient heart**
549 (a) Representative pictures of heart labelling using an antibody directed against the phosphorylated form
550 of RIPK1 at S161 from wild-type (WT) and dystrophin-deficient R-DMDdel52 rats. Quantification of
551 the rat *Ripk1* (d) and *Ripk3* (c) transcripts in hearts from WT and R-DMDdel52 rats. (d) Heart weights
552 of 18-month-old mdx mice. (e) Heart weights normalized to the tibial length (TL). (f) Quantification of
553 CD68-positive macrophage infiltrates. (g) Quantification of the density of CD31-positive microvessels,
554 (h) representative picture of Sirius red staining of mdx and mdx*Ripk3*$^{-/-}$. Scale bar: 1700 µm. (i)

Quantification of RV fibrosis. Hearts from 18-month-old mdx*Ripk3*$^{+/+}$ and $^{-/-}$ were analyzed for *Bnp* (j), and *Myh7* (k) mRNA levels by quantitative PCR. The normal distribution of data was tested using the Kolmogorov-Smirnov test (passing normality test with α=0.05), leading to either t-tests or Mann-Whitney tests. Data are given as means ± s.e.m. Ns: Not significant, *: p-value < 0.05, **: p-value < 0.01.

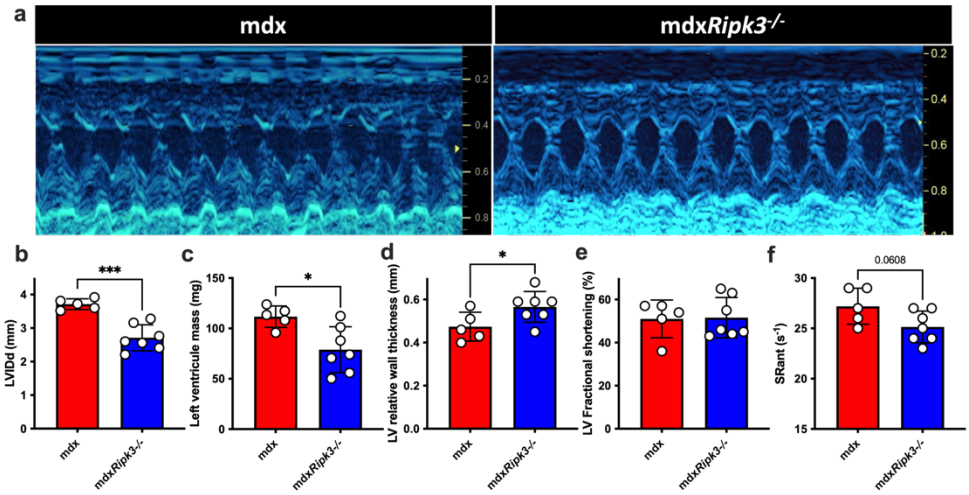

Figure 5: The genetic ablation of RIPK3 reduces cardiomyopathy in mdx mice

(a) Representative M-mode echocardiogram traces in mdx and mdx*Ripk3*$^{-/-}$ 40-week-old mice showing a reduced left ventricle (LV) dilation in mdx*Ripk3*$^{-/-}$ mice. (b) Quantification of LVIDd, (c) LV mass, (d) LV relative wall thickness, (e), LV fractional shortening, and (f) strain rate (SR) of the anterior LV wall. The normal distribution of data was tested using the Kolmogorov-Smirnov test (passing normality test with α=0.05), leading to t-tests. Data are given as means ± s.e.m. *: p-value < 0.05, ***: p-value < 0.001.

571 **Supplementary data**
572
573

		Measured values										Calculated values			
	Mouse#	Tibial length (mm)	Normalizing factor	HR, beats/min	IVSd, mm	IVSs, mm	LVIDd, mm	LVIDs, mm	PWd, mm	PWs, mm	SRant, s-1	LV RWT, mm	LV mass, mg	LVFS, %	LVEF, %
mdx	1	21.1	0.912	523	0.78	1.45	3.81	1.85	0.74	1.68	26	0.40	95.75	51	88
	2	18.2	1.056	605	0.94	1.64	3.92	1.70	0.76	1.49	29	0.43	117.26	57	91
	3	19.2	1.006	513	0.85	1.60	3.60	1.56	0.98	1.48	27	0.51	113.44	57	91
	4	19.1	1.011	535	0.86	1.88	3.52	1.63	1.13	1.88	25	0.57	123.85	54	89
	5	18.8	1.027	605	0.85	1.13	3.72	2.38	0.85	1.31	29	0.46	108.05	36	72
	Mean	19.3	1.0	556.2	0.9	1.5	3.7	1.8	0.9	1.6	27.2	0.5	111.7	50.9	86.2
	SD	1.10	0.05	45.22	0.06	0.28	0.16	0.33	0.16	0.22	1.79	0.07	10.60	8.65	8.04
mdx*Ripk3* -/-	1	18.1	0.932	545	0.74	1.43	3.28	1.48	0.75	1.26	24	0.45	101.18	55	91
	2	17.6	0.961	503	0.89	1.75	3.16	1.11	0.78	1.53	26	0.53	112.28	65	95
	3	17.8	0.950	609	0.79	1.56	2.76	1.03	0.85	1.30	24	0.59	87.89	63	94
	4	20.7	0.816	615	0.59	1.17	2.41	1.34	0.69	1.08	27	0.53	50.19	45	82
	5	19.7	0.855	650	0.74	1.17	2.21	1.19	0.76	1.06	27	0.68	55.91	46	84
	6	19.2	0.879	640	0.76	1.22	2.60	1.46	0.78	1.17	23	0.59	74.12	44	82
	7	18.4	0.915	634	0.76	1.35	2.56	1.46	0.76	1.38	25	0.59	70.62	43	80
	Mean	18.8	0.9	599.4	0.8	1.4	2.7	1.3	0.8	1.3	25.1	0.6	78.9	51.5	86.9
	SD	1.15	0.05	54.76	0.09	0.22	0.39	0.18	0.05	0.17	1.57	0.07	22.86	9.25	6.28

574

575 **Supplementary table 1: M-Mode echocardiographic values.**

576
577